

3D fast-mode Wave Propagation from Corona to Chromosphere: Triggering Mechanism for 3D Oscillations of filaments

YUNXUE HUANG ^{1,*} QIN FENG ^{1,*} YUHU MIAO ² ZHINING QU ¹ KE YU ¹ HONGFEI LIANG,³ YU LIU,⁴ AND XINPING ZHOU ¹

¹ College of Physics and Electronic Engineering, Sichuan Normal University, Chengdu 610068, People's Republic of China

² School of Information and Communication, Shenzhen Institute of Information Technology, Shenzhen, 518172, People's Republic of China

³ Department of Physics, Yunnan Normal University, Kunming 650500, People's Republic of China

⁴ School of Physical Science and Technology, Southwest Jiaotong University, Chengdu, 611756, Sichuan, China

ABSTRACT

Moreton waves are widely regarded as the chromospheric counterpart of extreme ultraviolet (EUV) waves propagating in the corona. However, direct observational evidence confirming their simultaneous propagation across multiple atmospheric layers—from the corona through the transition region to the chromosphere—has been lacking. In this study, we present comprehensive observational evidence of a three-dimensional (3D) fast-mode wave propagating from the corona through the transition region into the chromosphere, exhibiting a gradual deceleration. Additionally, this wave interacts with three filaments (F1, F2, and F3) along its path, inducing oscillation with multiple amplitudes: Filaments F1 and F2 exhibit simultaneous horizontal and vertical large-scale oscillations ($\sim 20 \text{ km s}^{-1}$), while Filament F3 only exhibits vertical small-scale oscillation ($\sim 4 \text{ km s}^{-1}$). Interestingly, F1 displays a similar oscillation period of about 500 s in both horizontal and vertical directions, whereas F2 shows significantly different periods in these two dimensions (1100 s and 750 s), and F3 exhibits only a vertical oscillation with a period of about 450 s. Based on this kinematic behavior, we propose that their oscillations were likely triggered by compression from the flanks of the dome-shaped wavefront. We further estimate the magnetic fields of the filaments. The radial (axial) magnetic fields for F1 and F2 are estimated to be 14.9 G (28.6 G) and 9.9 G (18.6 G), respectively. For F3, we estimate its radial magnetic field to be 16.6 G.

Keywords: Solar coronal waves(1995) — Alfvén waves (23) — Solar corona (1483)

1. INTRODUCTION

Moreton wave, flare-associated waves seen in $H\alpha$, rapidly propagating in restricted angles with speeds range from 550–2500 km s^{-1} (Moreton 1960; Warmuth et al. 2001; Asai et al. 2012; Liu et al. 2013). At some distance ($\sim 100 \text{ Mm}$) from the flare site, they often appear as arc-shaped fronts, with an angular width of about 100° , propagating away from the flare kernel which last for only minutes and soon become irregular and diffuse. As the waves were found to be too fast to originate in the chromosphere, Uchida (1968) developed a theory that interprets Moreton waves as the “hemline” of a dome-shaped magnetohydrodynamic (MHD) wavefront sweeping across the chromosphere. According to this model, the increased pressure behind the wavefront compresses the chromospheric plasma, which manifests as the characteristic down-up swing in $H\alpha$ filtergrams and has recently been confirmed via extreme ultraviolet (EUV) redshifts (Harra et al. 2011; Veronig et al. 2011) and direct EUV imaging (Liu et al. 2012; Chen & Wu 2011). The Extreme-ultraviolet Imaging Telescope (EIT; Delaboudinière et al. 1995) on board SOHO for the first time imaged such wave-like disturbance in solar corona (Thompson et al. 1998). Given that the Alfvén speed increases with altitude in the lower corona, the wavefront of a coronal fast-mode MHD wave is anticipated to tilt forward toward the solar surface. This inclination has been confirmed in several limb events, as documented by many studies (such as Ma et al. 2011; Cheng et al. 2012; Liu et al. 2012; Wang et al. 2020; Zhou et al. 2021). In certain numerical simulations, the Moreton waves have been successfully reproduced. For instance, the hybrid model developed by Chen & Wu (2011) demonstrates how piston-driven shocks, generated by expanding coronal mass ejections (CMEs), propagate through the chromosphere and produce

Corresponding author: Yu Liu
lyu@swjtu.edu.cn

Corresponding author: Xinping Zhou
xpzhou@sicnu.edu.cn

* These authors contributed equally to this work and should be considered co-first authors.

the Moreton wave signatures observed in $H\alpha$ emissions. However, no comprehensive images evidence simultaneously covering corona-transition region-chromosphere have been reported to date. It is worth noting that many of the coronal EUV wave studies revealed a close association with the CMEs (Chen et al. 2005; Chen 2006, 2009). However, some observation and simulations reveal that the energy release during the flare can drive the EUV wave train (e.g., Wang et al. 2021; Zhou et al. 2022a,c, 2024c). Furthermore, Zhou et al. (2024a,b) find that the EUV wave have close relationship with the untwisting of the erupting filament. These discrepancies indicate that we need to continue research on the origin of the EUV waves.

The EUV wave always interacts with the coronal magnetic structures, such as coronal holes (Li et al. 2012; Zhou et al. 2022b, 2024d; Zhang et al. 2025), active regions (Miao et al. 2019), filaments (or prominences) (Li & Zhang 2012; Liu et al. 2013), coronal loops (Srivastava et al. 2013; Srivastava & Goossens 2013; Zhang et al. 2022) and coronal cavity (Zhang & Ji 2018; Liakh et al. 2023; Liakh & Keppens 2023). Following this interaction, filaments (or prominences) are always observed to exhibit oscillations. According to the oscillation direction, the filament oscillations can be divided into three categories, namely longitudinal oscillation (e.g., Luna & Karpen 2012; Zhang et al. 2012, 2013; Luna et al. 2014; Bi et al. 2014; Shen et al. 2014b; Zhang et al. 2017b, 2020b; Liakh et al. 2021; Luna et al. 2024; Yan et al. 2025), transverse horizontal (e.g., Kleczek & Kuperus 1969; Gosain & Foullon 2012; Zhang 2020; Zhang et al. 2024) and transverse vertical (Hyder 1966; Shen et al. 2014a). In recent years, the simultaneous observations of two or more mixed oscillation modes have also attracted attention, like simultaneous transverse and longitudinal oscillations (Zhang et al. 2017a; Mazumder et al. 2020; Tan et al. 2022, 2023), or simultaneous horizontal and vertical oscillations (Dai et al. 2023; Ouyang et al. 2025). When the filaments are not at the solar limb, their oscillation will exhibit an interesting phenomenon in the line-of-sight (LOS) direction, namely the “winking” phenomenon, which is characterized by their gradual fading or complete disappearance followed by subsequent reappearance in $H\alpha$ line wings. Traditionally, “winking” oscillations have been considered vertical (Tripathi et al. 2009). However, this characterization is accurate only when the filament is located near the disk center. For filaments closer to the limb, the oscillations may have a significant horizontal component. In this work, we use the term vertical for simplicity, although we actually refer to motions along the line of sight. Notably, the observed oscillation periods primarily correlate with the filaments’ intrinsic characteristic periods, showing no significant correlation with the physical dimensions of the filaments, nor with the proximity and energy magnitude of the triggering flare events. Ramsey & Smith (1966) and Hyder (1966) studied 11 winking filaments, deriving oscillatory periods ranging from 6 to 40 minutes and damping times between 7 and 120 minutes. They suggested that each filament has its own characteristic frequency of oscillation, noting that a filament perturbed by waves from four flares over three consecutive days oscillated with essentially the same frequency and damping time, further emphasizing the lack of correlation between the oscillation frequency and the filament dimensions, the distance to the perturbing flare, or its size. This finding was further confirmed by Hershaw et al. (2011), who proposed that large-amplitude filament oscillations are actually a collection of separate but interacting fine threads. Oscillations triggered by Moreton or coronal waves often exhibit large amplitudes ($>20 \text{ km s}^{-1}$; see the review by Tripathi et al. 2009), in contrast to the commonly observed small-amplitude oscillations ($\sim 2\text{--}3 \text{ km s}^{-1}$; see the review by Arregui et al. 2018), which are typically local and appear intrinsic to the filament itself, lacking any obvious external trigger. The physical mechanism underlying wave-filament interactions remains poorly understood due to the relative scarcity of observational data. Notably, filaments do not always exhibit oscillatory behavior when waves pass through them (Okamoto et al. 2004).

Despite the fact that EUV waves have been frequently observed in the solar corona for over a decade, their counterparts in the chromosphere are rarely detected (Zheng et al. 2023). Moreover, comprehensive observational evidence of their propagation through various atmospheric layers is still lacking. According to the statistic 640 coronal EUV waves from 2010 to 2021 by Wang et al. (2025), they find that only 92 events (accounting for $\sim 14.4\%$) exhibit responses in the transition region, and among these 92 events, only 20 (accounting for $\sim 3\%$) showed chromospheric response. Typically, in wave-filament interactions, the material undergoes vertical oscillations with respect to the solar surface. In addition, simultaneous horizontal and longitudinal oscillations of a filament have been reported. However, the simultaneous horizontal and vertical (winking phenomenon) oscillations in filaments were rarely reported in previous studies. In this paper, we present observational evidence of a coronal wave propagating from the corona to the chromosphere, and causing the filaments’ three-dimensional oscillations. Section 2 briefly introduces the observation instruments. Section 3 analyzes the propagation of the wave and the oscillations of the filaments. Section 4 presents the discussion and conclusions.

2. OBSERVATIONS

An intense flare, GOES X5.8, occurred in the active region NOAA 13664 on 11 May 2024. The flare started at 01:10 UT, peaked at 01:23 UT and ended at 01:39 UT. We observed a coronal EUV wave, accompanied by a Moreton wave, associated with the flare in the Atmosphere Imaging Assembly (AIA; Lemen et al. 2012) EUV images and $H\alpha$ images obtained from the Solar

Magnetic Activity Research Telescope (SMART; UeNo et al. 2004). The wave triggers multiple mini filament oscillations both in the EUV and $H\alpha$ images. For analyzing the EUV wave and horizontal filament oscillations, we utilized the high spatio-temporal resolution observational data from AIA on board the Solar Dynamics Observatory (SDO; Pesnell et al. 2012). The AIA takes full-disk images at seven EUV wavebands that can observe the sun from chromosphere to corona. It is well known that both the Chinese $H\alpha$ Solar Explorer (CHASE; Li et al. 2019, 2022) and SMART (UeNo et al. 2004; Ishii et al. 2013) instruments are capable of providing full-disk Doppler images. Unfortunately, CHASE was not operating during the period of this eruption event. Therefore, we mainly relied on data obtained from SMART to study the Moreton wave and the vertical oscillation of filaments using the Cloud Model (Beckers 1964). SMART regularly provides the full-disk Sun in seven wavelengths around the $H\alpha$ line (6562.8 Å), i.e., $H\alpha$ center and six off-band (± 0.5 Å, ± 0.8 Å and ± 1.2 Å) with a time cadence 2 minutes and pixel size $0''.56$. Such full-disk and multi-wavelength observation with high cadence is suit to detect Moreton waves in the chromosphere. SUTRI utilizes the 465 Å waveband to conduct full-disk dynamic imaging observation of the solar transition region (the layer between the solar chromosphere and corona) with a spatial and temporal resolutions of about $8.''0$ and 30 s, respectively (Tian 2017; Bai et al. 2023), thereby establishing a crucial bridge between the lower and upper solar atmosphere for observing the EUV wave.

3. RESULTS

3.1. The EUV wave and Moreton wave

Figure 1 shows the wave evolution observed in the corona by AIA 211 Å ((a)-(c)), transition region by SUTRI 465 Å and chromosphere by AIA 304 Å and SMART $H\alpha$ center images, using the running difference images. The wave was seen from about 01:13 UT to 01:26 UT with all AIA images and propagated forward to the northeast, during this 13 minutes. Comparing the spatial structure of the wave in different bands, we can find that the Moreton wave (marked with a white dotted curve in Figure 1 (e)), observed in $H\alpha$ image, is well coincident with the sharp bright wavefront captured in EUV bands, during the initial stage (see panels (a), (d), (e) and (f) in Figure 1). It is worth mentioning the shape of the Moreton wave in chromosphere is slightly smaller than that of the EUV wave in the corona, which was restricted to propagate within a smaller angular range, as shown in panel (a), (e) and (f) of Figure 1. Additionally, we observed an expanding dome (marked with a white dotted curve in Figure 1 (c)) that smoothly merged with the sharp one. This indicates that the EUV should be in a dome shape. These observation features support the theory proposed by Uchida (1968) that the expanding dome is thought to be the shock, the Moreton wave and the sharp EUV wave are the tracks when it intersection with the chromosphere and solar corona, respectively. As shown in Figure 1 (a)-(c), three coronal holes (CHs), marked with gray curves, were scattered around the eruption origin, and three filaments (F1, F2 and F3) (see the box in panel (d) observed by CHASE $H\alpha$) on the path of the wave propagation. Please refer to the animation of Figure 1 for the details about the EUV wave and Moreton wave.

We examined temporal features of the EUV and Moreton wave by using the time-distance stack plots following a sector marked with S1 in Figure 1 (a), which are drawn with a great circle of the solar surface from the flare kernel. Here, we only show the evolution process of the wave in the direction, i.e., S1, towards the mini filaments on northwestern limb (see Figure 1 (a), where the filament shapes obtained from the CHASE $H\alpha$ observation are overlaid on it). Figure 2 is the time-distance stack plots reconstructed follow S1 using running difference images (except for panel (f), which uses AIA 335 Å raw images because its wave signal appears more prominently). Obviously, we can observe an inclined bright ridge in each panel, representing the wave signals propagating from the chromosphere through the transition layer to the corona. The wave is very bright and sharp from 01:14 UT to 01:22 UT, which is almost the same time range as the Moreton wave. The slope of these ridges corresponds to the speed of the wavefront. By performing a second-order polynomial fitting, we obtained the propagation speed and deceleration of the wavefront at various atmospheric heights. As shown in Figure 2, we can see that the wave propagating speeds observed in 211, 193, 171, 94, 131 and 335 Å (with a average value of about 940 km s^{-1}), which are significantly higher than the speed observed in 304 Å which was about 720 km s^{-1} (see Figure 2 (g)). As AIA 304 Å channel primarily encompasses the He II 303.8 Å line, dominate at chromosphere temperatures of $\log(T/K) \sim 4.7$. Thus, we believe that the signal observed in the 304 Å band represents the signatures of the wave propagation in chromosphere. This can be verified from the observations in the SMART $H\alpha$ band. As shown in Figure 2 (i), we can see that the wave propagation speed in chromosphere observed in SMART $H\alpha$ was about 720 km s^{-1} , which is consistent with that observed in AIA 304 Å. Furthermore, we find that the wave propagation speed in the transition region was about 770 km s^{-1} observed in SUTRI 465 Å band (see Figure 2 (h)). This speed is higher than that measured in the chromosphere (720 km s^{-1}) but lower than the corona value (940 km s^{-1}). This difference in speed further reflects that the wave front has dome-like shape: as the height increases, the projected speed become greater, a conclusion has been verified in other literature (Liu et al. 2012).

3.2. The horizontal oscillations of the filaments

As the wave propagating about 400 Mm arrived near the filaments on the west limb, it triggered the filaments to begin oscillating (see Figure 2 (g)). We selected a series of straight slice to investigate the oscillation of the filaments in the plane-of-sky (POS) direction, (i.e., the transverse horizontal oscillation). The left panels of Figure 3 is a close up region of the mini filaments in the AIA 171 Å, CHASE H α , and SMART H α , where three mini filaments, F1, F2 and F3, can clearly be identified. We draw three sets of straight lines (Figure 3 (a1)–(a3)), overlaying on the corresponding filament, to study their oscillation in the directions perpendicular to their axes. The starting of lines for F1 and F3 are located at the center of the circle. Since the axis of F2 is difficult to distinguish, we took its centroid as the center and draw 12 diameters at 15° intervals to analysis its oscillation in the POS. The starting points of each diameter is marked with a solid dot at its end. From the time-distance stack plots shown in Figure 3 (b1)–(b3) derived from raw AIA 171 Å images, we found that filaments F1 and F2 exhibited significant oscillations. These oscillations commenced around 01:22 UT, and lasted for 5 and 3 cycles, respectively. In contrast, filament F3 remained stationary during this period. To obtain the oscillation parameters, we fit the oscillation profile with a damping function in the form of $f(t) = Ae^{(-t/\tau)}\cos(2\pi/T + \phi)$, where A , T , τ , and ϕ are the initial amplitude, period, damping time, and initial phase, respectively. The fitting results reveal that filament F2 exhibits an oscillation period of 1108 s and a amplitude of 2.5 Mm, both of which are significantly larger than those of filament F1 (520 s and 1.5 Mm, respectively). All time-distance stack plots results can be found in Figure 6 and Figure 7 of the Appendix. We also employ this fitting method to derive the vertical oscillation parameters (see Figure 5).

3.3. The vertical oscillations of the filaments

Figure 4 presents the time sequence of SMART H α line-center and line-wind images to illustrate the motion of the filaments in the LOS direction at three different stages. The middle column shows the H α line-center images, while the left (right) column display the images in the blue (red) wings (± 1.25 Å and ± 0.5 Å), respectively. The first row presents the state of the filaments before the oscillation begins, and these three filaments can be clearly seen in the H α center image (see panel (a3)). Around 01:22 UT, F1 and F2 appear in the red wing images (see Figure 4 panels (b3)–(b5)), suggesting that these two filaments undergo a downward motion. Meanwhile, the intensity of F1 and F2 decreases in the H α center image. As the wavelength increases, the intensity of the filaments decreases. In the H α +1.25 Å image, F2 can still be seen while F1 disappears. Approximately seven minutes later, F1 and F2 appear in the blue wing images (see Figure 4 panels (c1)–(c3)), indicating that they start to move upward. F1 is visible in the image H α –0.5 Å but its intensity is lower than that of F2. In the H α –1.25 Å image, F1 disappears completely while F2 is still partially visible. Compared to filament F1 and F2, the winking signal of filament F3 is relatively less obvious: only some faint signals can be find in red wing (panel (b4)) and blue wing (panel (c2)).

To obtain the detailed parameters of vertical oscillation of these filaments, we select four sample points on F1–F3 respectively (marked by white cross points in Figure 4 panel (a3)) for Doppler velocity. To obtain the Doppler velocity of the filament, we first measure the intensity contrast profile of a sample point on the filaments by dividing the nearby average background intensity (marked with green cross in Figure 4 panel (a3)). Subsequently, we fit the derived intensity contrast profile using the cloud model (Beckers 1964) to determine the corresponding Doppler velocity of the sample points. The detailed analysis results of the three filaments' oscillations along the LOS is shown in Figure 5. The blue curves in each panel are the Doppler velocities acquired from four sampling points of filaments F1, F2 and F3, respectively. These periodic fluctuations observed in the velocity measurements demonstrate the oscillatory motion of the filaments in the LOS direction. Additionally, it is evident that both filaments, F1 (panels (a1)–(a4)) and F2 (panels (b1)–(b4)), initially exhibit a stronger redshift signal when the wave approaches them around 01:22 UT. Afterward, blueshift and redshift alternate. This evolutionary pattern suggests that the wave first pushed the filaments downward due to a strong compression originating from its dome-shaped propagating wavefront. Following the passage of the pulse, the filaments begin to oscillate with their own characteristic period. By fitting the detrended Doppler velocities using the same method mentioned in Figure 3, we find that: the period for F2, approximately 740–780 s, is significantly longer than that of F1, which is around 470–520 s. In contrast, the velocity amplitude for F1, ranging from 12 to 24 km s^{–1}, is slightly higher than that of F2, which ranges from 19 to 21 km s^{–1}. Notably, the four sample points of F2 were relatively concentrated in the central region of filament F2, resulting in approximately identical oscillation start times observed in the Doppler velocity map. However, the four sampling points of F1 were distributed along the filament axis from left to right, leading to a continuous variation in the oscillation onset times. For filament F3, its left portion exhibited significant oscillations with amplitudes of 3.8 to 5.5 km s^{–1} and periods of approximately 415–485 s (see Figure 5 (c1) and (c2)). In contrast, its right portion showed no significant oscillation. Since the oscillation onset at the two left sampling points (01:22 UT) coincided with the wave's arrival and their amplitudes were considerably larger than those at the two right points, we consider the left two points to accurately reflect the oscillation of filament F3, despite minor oscillatory signals also being present at the right two points.

4. DISCUSSION AND CONCLUSIONS

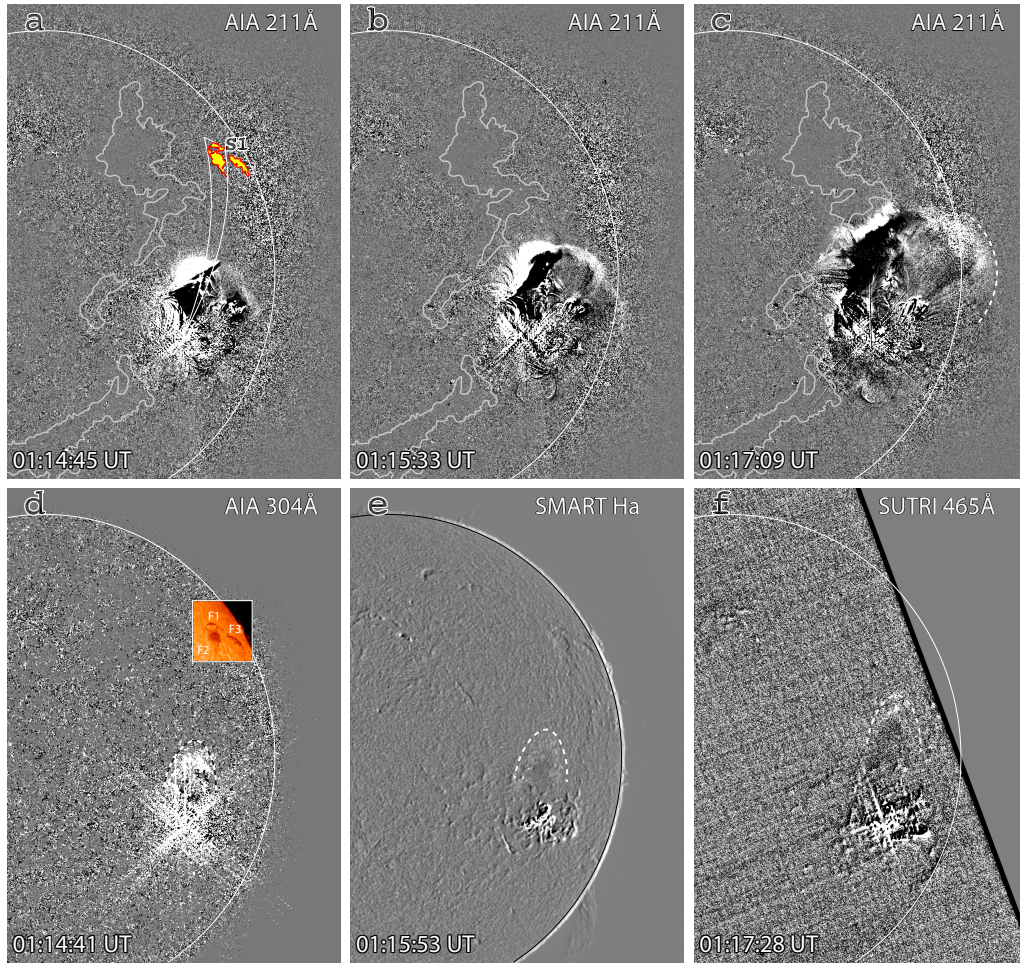


Figure 1. Overview of the EUV wave and Moreton wave. Panels (a)-(d) are the running difference of the AIA 211 Å and 304 Å images showing the EUV wave. Panel (e) exhibits the Moreton wave in SMART H α image, while panel (f) displays the EUV wave at SUTRI 465 Å running difference image. The wave front in AIA 304 Å, SUTRI 465 Å, and SMART H α image is highlighted with white arrows. The color box in panel (d) displays the mini filaments observed by CHASE H α . The closed curves in Panels (a)-(c) marked the location of the CHs, while the sector (labeled with S1) in panel (a) is used to obtain the time-distance stack plots in Figure 2. An online ~ 2 s animation which includes 335 Å, 304 Å, 211 Å, 171 Å, 131 Å, 94 Å, SUTRI 465 Å and SMART H α running-difference images covering 01:13 UT to 01:25 UT is available to view the details about the EUV wave and Moreton wave.

In this paper, we report a dome-shaped wave that was observed simultaneously in different layers of the solar atmosphere, which triggers oscillations in three filaments with varying amplitudes: two exhibit large-scale oscillations, while one shows small-scale oscillations. In the initial stage, the EUV wave observed in AIA/SDO EUV wavebands, the surface part of the wave, was co-spatial with the Moreton wave observed in the chromosphere using the SMART H α images. We also detected the wave signals in the transition region between the chromosphere and corona using SUTRI 465 Å images, which have often been overlooked in previous studies. During the free propagation stage, the speed of the wave increases with the height: it is about 720 km s^{-1} in the chromosphere, 770 km s^{-1} in the transition region, and 940 km s^{-1} in the corona. This difference in speed indicates that the wave has a dome-shaped. After propagating about 400 Mm, it interacted with three filaments along its propagation path, causing the first two to exhibit oscillation simultaneously in both horizontal and vertical directions, while the third one only oscillated in the vertical direction. Interestingly, both F1 and F2 were large-scale oscillations with a velocity amplitude about 20 km s^{-1} , while F3 was just oscillated on a small scale with an amplitude about 4 km s^{-1} . The vertical oscillations of filaments F1, F2 and F3 result in the winking behavior in the H α observations. The oscillation periods in horizontal and vertical of filament F1 are both approximately 500 s. In contrast, for filament F2, the periods show a significant difference, with values of 1100 s and 750 s, respectively. Filament F3 only exhibits oscillation in the vertical direction with a period of about 450 s.

Moreton waves in the chromosphere and EUV wave in the corona are intriguing large-scale phenomena in the solar atmosphere. Since the Alfvén speed in the chromosphere is approximately 100 km s^{-1} , the Moreton waves in the chromosphere cannot prop-

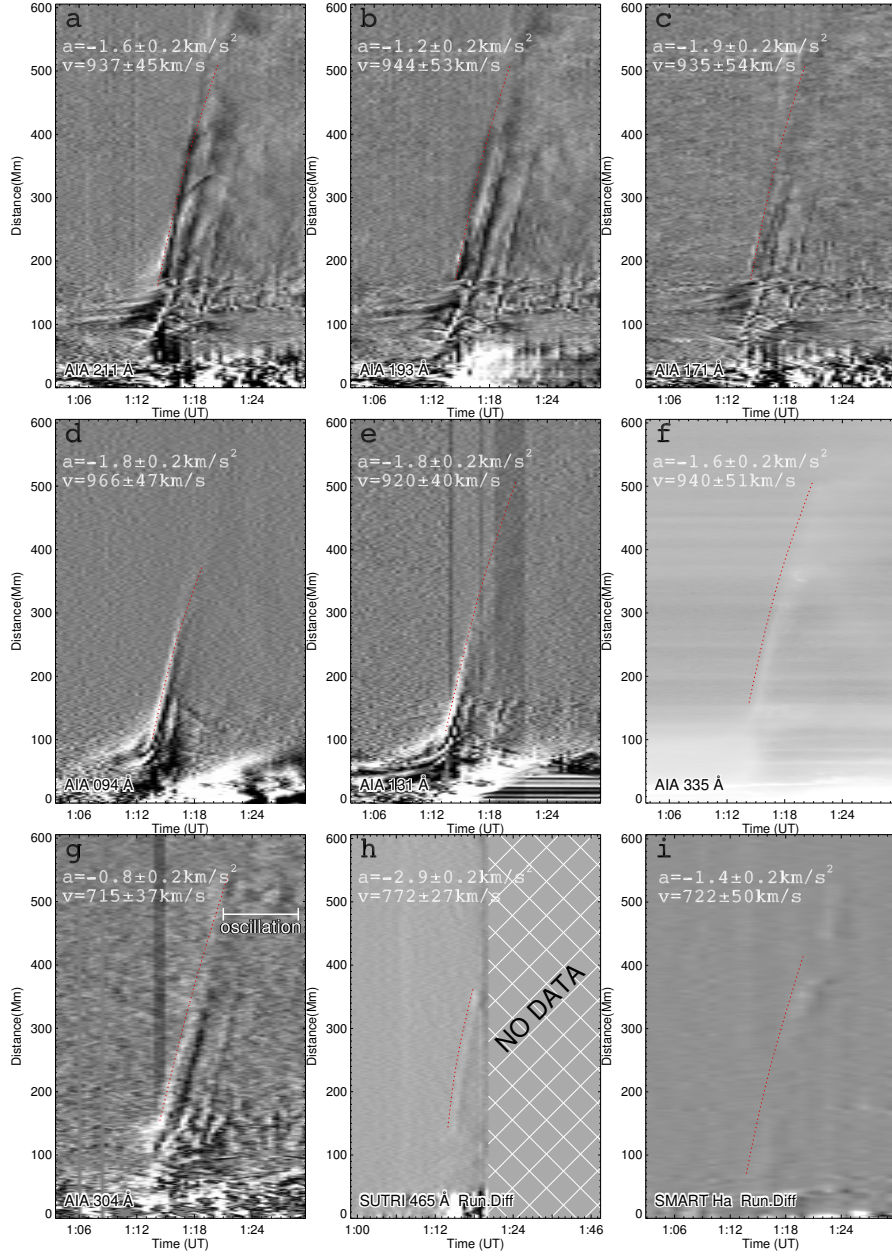


Figure 2. Time-distance stack plots showing the evolution of the EUV wave and Moreton wave, as obtained from the AIA 211 Å, 193 Å, 171 Å, 94 Å, 131 Å, 304 Å, and 335 Å, SUTRI 465 Å as well as SMART H α . The deceleration and initial speed of the wave obtained by fitting the spines in the time-distance stack plots are listed in corresponding panels, where the red dotted curved lines are the fitting results using a second-order polynomial function. Panel (g) marks the oscillations of filaments.

agate to a distance of about 100 Mm at a speed of approximately 1000 km s^{-1} . Instead, the waves will rapidly dissipate because of the excessively high Mach number. Uchida (1968) proposed that the pressure pulse from a flare generated a dome-shaped fast-mode wave or shock wave in the corona, propagating outward at a speed of approximately 1000 km s^{-1} . The base of the wave sweeps across the chromosphere, generating a Moreton wave. In other words, the Moreton wave is the imprint of the base of the fast-mode wave or shock wave in the corona on the chromosphere. The coronal wave, i.e. EUV wave, has been extensively studied in the past twenty years. Their physical nature and driven mechanism have finally been unified, namely, they are a fast-mode magnetosonic wave driven by the lateral expansion of the accompanying CMEs (Chen et al. 2002; Ma et al. 2011; Li et al. 2012; Miao et al. 2020; Hou et al. 2022; Chen 2023b). Although the model of Uchida (1968) is widely accepted, observations indicate that most EUV waves are not accompanied by Moreton waves. Regarding this issue of Moreton waves

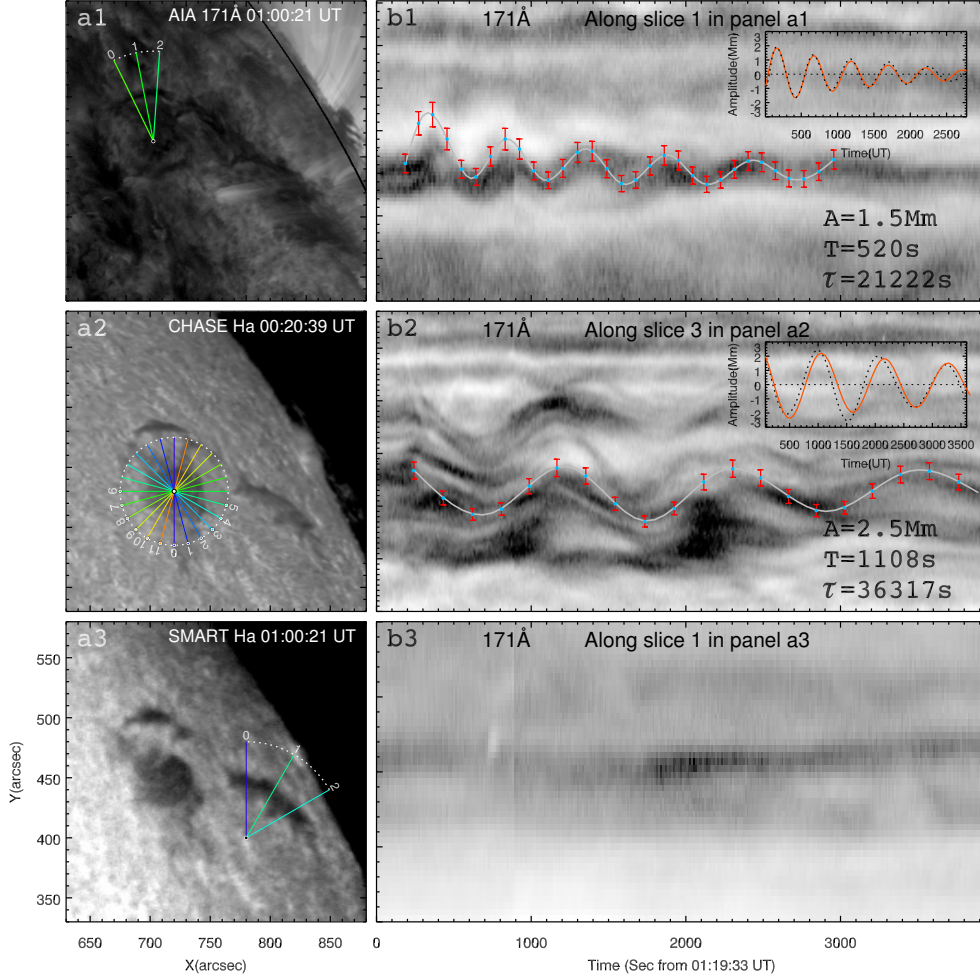


Figure 3. The horizontal oscillation of the filaments. Panels (a1)-(a3) show the filaments in AIA 171 Å, CHASE H α and SMART H α images, where the color lines marked the path to get time-distance stack plots to study their oscillation in different directions. In panel (a1) and (a3), the paths start at the center of the circle, while in panel (a2), the paths separated by 15° angle are located on the arc and are marked with solid circular dots. Panel (b1) shows the horizontal oscillation of filament F1 along the slice 1 in panel (a1). Panel (b2) is an example of the filament oscillation in the direction of slice 3 in panel (a2), while panel (b3) is an example of filament F3's oscillation in direction of slice 1 of panel (a3). The gray curves in panel (b1) and (b2) are the oscillation curve that manually marked the positions using for fitting. The black curve is the detrended of curve of the oscillation curve obtained by subtracting the smooth velocity using a 10 minutes boxcar, where the red curve is its fitting result using the formula $f(t) = Ae^{(-t/\tau)}\cos(2\pi/T + \phi)$. The fitting results are listed in corresponding panel.

being rarely observed, Zheng et al. (2023) found that EUV waves and Moreton waves exist only in eruptions that are sufficiently inclined. The AIA 304 Å images show that the ejection of the filament reported here erupted obliquely towards the northwest, leading to the generation of the Moreton wave propagating in the same direction. This is consistent with the result proposed by Zheng et al. (2023). Chen et al. (2022, 2024) conducted numerical experiments to investigate the cause of the inclined eruption of the filament, discovering that the occurrence of a catastrophe in an asymmetric and non-force-free environment is the primary reason for this phenomenon. We anticipate future numerical simulation of non-radial eruptions leading to the Moreton waves. This would enable a more detailed study of the relationship between the Moreton wave and the erupting filaments.

According to the theoretical interpretation in Uchida (1968), the shock wave has a dome-shaped structure and appears as a circular shape when projected onto the solar disk. When this shock wave intersects with the chromosphere, it will lead to the formation of the Moreton wave. This raises the question: since the transition between the corona and chromosphere is inevitable for the propagating shock, one would expect to observe wave signals in this region as well. However, in reality, little attention has been paid to such wave signals in the transition zone. The wave, reported here, was simultaneously observed in the AIA EUV wavebands, SUTRI 465 Å and SMART H α images, covering a broad temperature range from the low corona, transition

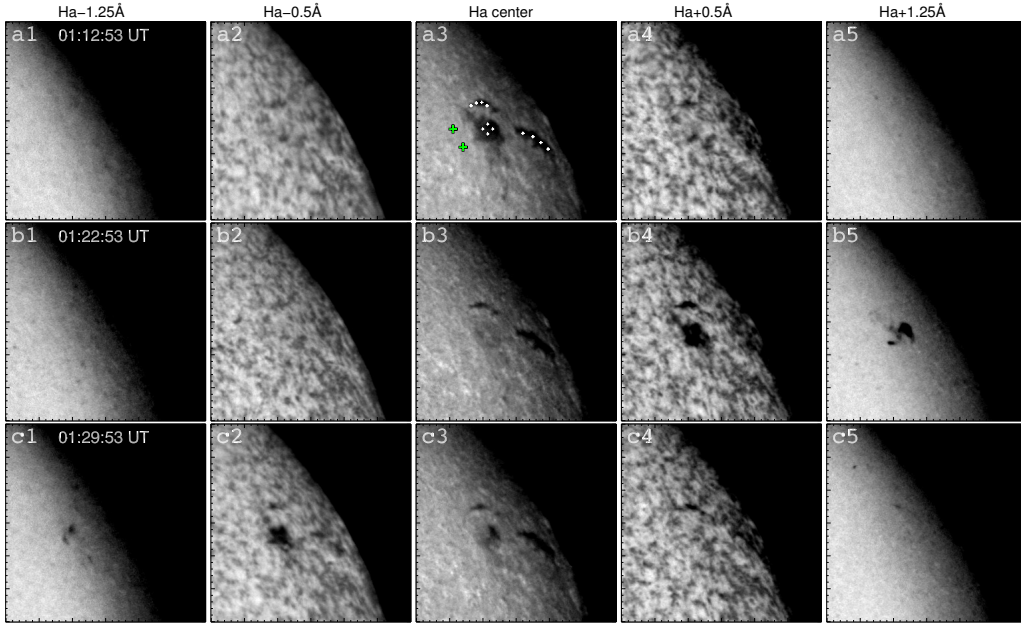


Figure 4. Time sequence of SMART $H\alpha$ images show the oscillation of the filaments in the LOS direction at three different time. The five columns, from left to right, represent images from bands -1.25 \AA , -0.5 \AA , 0.0 \AA , $+0.5 \text{ \AA}$ and $+1.25 \text{ \AA}$ images shifting from the $H\alpha$ line center (6562.8 \AA), respectively. Images in the same row are taken at a near simultaneous time refer with the $H\alpha$ center image. The four white marked points on F1, F2 and F3 in panel (a3) are the positions where Doppler velocities are measured, while the two green points are used to get the background intensity.

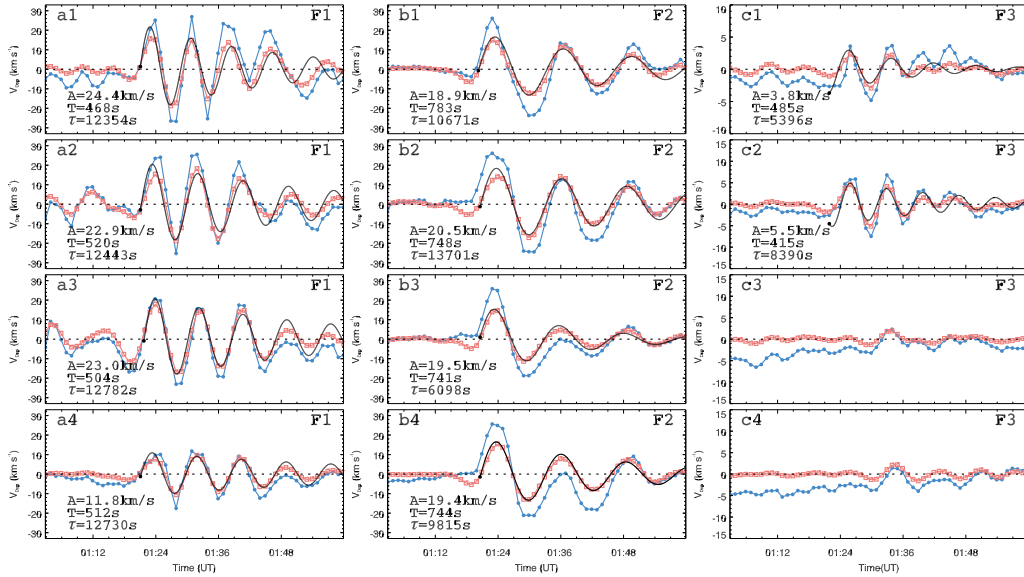


Figure 5. Measurement of the Doppler velocity of the oscillation filaments. The Doppler velocities obtained from sampling points on filaments F1, F2 and F3 are shown in (a1)-(a4), (b1)-(b4) and (c1)-(c4), respectively. In each panel, the blue curve with circle dot is the derived Doppler velocity, while the red curve with diamond is the detrended velocity. The back curve is a fit to the detrended velocity using the formula $f(t) = Ae^{(-t/\tau)}\cos(2\pi/T + \phi)$. The fitted velocity amplitude (A), oscillation period (T) and damping time (τ) are listed in corresponding panel.

region, to the chromosphere, indicating that the EUV wave and its chromospheric counterpart, namely, Moreton wave, as well as the response in the transition are observed. Notably, we find that a decreasing wave speed in the initial phase, moving from the lower corona towards the chromosphere: about 940 km s^{-1} in the corona, 770 km s^{-1} in the transition region, and 720 km s^{-1} in the chromosphere. This is probably a result of the dome-shaped wavefront structure, causing a delay in the disturbance reaching the lower atmosphere. The expanding dome-shaped of the EUV always gets the evidence from the limb observation in previous

observation (Ma et al. 2011; Cheng et al. 2012; Liu et al. 2012; Zhou et al. 2021). In this study, we present the first empirical verification of the wave front's geometry achieved by analyzing the velocity differences at different solar atmospheric heights.

Large-amplitude oscillations (greater than 20 km s^{-1}) are the periodic motions of the entire filament (or most of it) body often associated with Moreton waves or EUV waves (e.g., Eto et al. 2002; Gilbert et al. 2008; Gosain & Foullon 2012; Asai et al. 2012; Liu et al. 2013; Dai et al. 2023). The earliest reported observations of filament oscillation can be traced back to the 1930s (Newton 1935). Although horizontal and vertical oscillation of filaments has been widely studied, the simultaneous horizontal oscillation and the winking phenomenon in a filament has rarely been reported (Luna et al. 2018). To the best of our knowledge, only a few of papers have reported the simultaneous presence of similar horizontal and vertical oscillation in a filament: Isobe & Tripathi (2006), Dai et al. (2023) and Ouyang et al. (2025). Since the filament was located far from the disk center in the southern solar region, the horizontal oscillation reported by Isobe & Tripathi (2006) is subject to considerable uncertainty due to foreshortening effects, as already noted by the original authors. Moreover, given the relatively low resolution of available observational data, it is quite difficult to accurately determine filament position changes based solely on two images. In contrast, using SMART H α line-wing observations, Shen et al. (2014a) detected successive episodes of filament winking. Interestingly, while these filaments exhibited clear vertical oscillations in the SMART data, they showed neither transverse horizontal nor longitudinal oscillations in the simultaneous high-resolution observations from AIA/SDO. Dai et al. (2023) and Ouyang et al. (2025) provided evidence for simultaneous horizontal and vertical oscillations. However, along the LOS direction, they only presented velocity parameters without explicit information regarding oscillations.

A significant application of filament oscillations and coronal seismology is to calculate parameters such as the ambient magnetic field that cannot be directly measured (e.g., Shen et al. 2014a; Luna et al. 2018; Dai et al. 2023; Zhang et al. 2020a; Li et al. 2023). Only based on the correct analysis of the oscillation modes can we calculate the corresponding magnetic field using relevant parameters. By using the formula for vertical oscillation of filament given in Hyder (1966):

$$B_r^2 = \pi \rho r_0^2 \left[4\pi^2 \left(\frac{1}{T} \right)^2 + \left(\frac{1}{\tau} \right)^2 \right]$$

We can obtain the radial component of the magnetic field B_r , where $\rho = N_H m_H$ (N_H and m_H are the average number density and mass of hydrogen atom respectively) is the density of the filament material, r_0 is the scale height of the filament, T is the vertical oscillation period of the filament, and τ is the decay time. We can substitute $m_H = 1.67 \times 10^{-24} \text{ g}$, $N_H = 3 \times 10^{10} \text{ cm}^{-3}$ (Labrosse et al. 2010), $r_0 = 3 \times 10^9 \text{ cm}$ (Hyder 1966), and the measurement data from this event into the formula for calculation. According to the fact that the vertical oscillation average periods of F1, F2 and F3 are 501 s, 754 s, 450 s; the mean decay time are 12577 s, 10071 s and 6893 s, we can calculate that the value of B_r at the position of F1, F2 and F3 is 14.9 G, 9.9 G and 16.6 G, respectively. This value falls within the range of 2–30 G provided by Hyder (1966) and is also fairly consistent with previous research results (Shen et al. 2014a; Luna et al. 2017; Dai et al. 2023). According to the period equation for horizontal oscillation given by Kleczek & Kuperus (1969):

$$P = 4\pi L B_l^{-1} \sqrt{\pi \rho}$$

Among them, P refers to the period of horizontal oscillation, $2L$ is the length of the filament, ρ , as mentioned above, is the density of the filament. By substituting the measured period of 525 s (1115 s) for the F1 (F2) horizontal oscillation and the estimated length 60.19 Mm (83.10 Mm) (detailed measurement methods in the Appendix), we can calculate the magnetic field strength at the position of F1 (F2) along axial direction of the filament to be 28.6 G (18.6 G).

The interaction mechanism between solar filaments and waves is an important and complex issue. Shen et al. (2014b) proposed a simple model where the oscillation mode (transverse or longitudinal) depends on the relative orientation of the wave normal vector and the filament axis: transverse oscillations occur if the normal vector is perpendicular to the axis, while longitudinal oscillations occur if it is parallel. However, this simple picture is challenged by observations. For example, Shen et al. (2014a) reported a case where the filament F1 was parallel to the wave normal vector, filaments F2, F3, and F4 were perpendicular to the wave normal vector, yet only vertical oscillations were observed, with neither longitudinal nor horizontal oscillations detected. Similarly, Zhang & Ji (2018) found only vertical oscillations in a filament where the wave normal vector was perpendicular to the filament axis. These contradictory observations demonstrate that the wave-filament interaction is still a complex issue and requires further investigation, particularly through numerical simulations and multi-wavelength, multi-viewpoint observations. To the best of my knowledge, only a few numerical simulations have focused on this complete process, from wave generation and propagation to its interaction with distant filaments, such as Liakh et al. (2020) and Liakh & Keppens (2025). We anticipate that further 3D simulations of the wave-filament interaction will offer more detailed insights into their interaction process.

In this study, our simultaneous AIA and SMART observations of filament F1 reveal a similar oscillation period of approximately 500 s in both the apparent horizontal and vertical directions. Furthermore, both apparent oscillations exhibited 5 cycles

with nearly identical onset times, around 01:22 UT. Based on these similarities, we make the bold conjecture that filament F1 might, in fact, undergo only genuine vertical oscillations relative to the solar surface. The apparent horizontal oscillation could then be a projection effect. This conjecture is supported by previous findings, such as those by [Shen et al. \(2014a\)](#) and [Zhang & Ji \(2018\)](#), who reported observing exclusively vertical oscillations in filaments located near the disk center and at the limb, respectively. These results lend credence to the idea that the apparent horizontal oscillation of filament F1 reported here might be solely due to the projection of its underlying vertical motion. This highlights a key challenge: the same intrinsic oscillation mode can manifest as different observed behaviors depending on the filament's location and orientation relative to the observer. Consequently, accurately determining the true oscillation mode and mechanism is particularly difficult when observing from a single viewpoint and in a single spectral band.

In contrast, filament F2 exhibited a significant difference in oscillation periods between the apparent horizontal and vertical directions. This difference strongly suggests that F2 underwent genuine, distinct horizontal and vertical oscillations, rather than a single projected motion. As confirmed in Appendix Figure 7, analysis of 12 slices around F2 revealed oscillation signals in multiple directions. The most prominent signals were observed in slices 6, 7, and 8, indicating that horizontal oscillation was the dominant component among the observed motions. Regarding filament F3, it exhibited a small-scale oscillation in vertical direction with a velocity amplitude about $3.8\text{--}5.5\text{ km s}^{-1}$ in its left portion, which is consistent with previous reports indicating that the small-scale oscillations have local characteristics ([Tsubaki & Takeuchi 1986](#); [Balthasar et al. 1993](#); [Terradas et al. 2002](#); [Berger et al. 2008](#)). Generally, small-amplitude oscillations are not related to an external trigger ([Arregui et al. 2018](#)). However, we propose that the small-amplitude oscillation of filament F3 reported here was triggered by the Moreton wave as its onset oscillation coincided with the arrival of the Moreton wave.

In conclusion, the excellent spatial and temporal resolution of the observations presented here provides a better understanding of the physical properties of filaments, EUV waves, and Moreton waves. These insights offer potentially valuable inputs and constraints for theoretical models. Furthermore, as the Sun progresses through solar cycle 25 and approaches its maximum activity ([Chen 2023a](#)), it presents a prime opportunity to study the interactions between Moreton waves and filaments.

APPENDIX

A. THE HORIZONTAL OSCILLATION OF THE FILAMENTS

As shown in Figure 3, we selected three sets of paths for space-time analysis. Since the spines of filament F1 and F3 were easy to be identified, we select 3 paths perpendicular to the filament axis for filament F1 and F3 respectively to detect their oscillation in horizontal directions. However, it is difficult to judge whether the filament F2 oscillation is along axis direction or perpendicular to it. Thus, we placed 12 slices centered on the filament mass F2 in different directions, where the 12 directions are uniformly distributed in the azimuthal directions as shown by the color solid lines in panel a2 of Figure 3, using the method proposed by [Chen et al. \(2017\)](#) and further developed by [Tan et al. \(2023\)](#). The corresponding time-distance stack plots of 171 \AA images along these slices are shown in Figure 6 and Figure 7. The starting points of these paths are all marked with solid small dots located at one of their endpoints.

As illustrated in Figure 6, filament F1 exhibits significant oscillations in all three directions, while filament F3 remains stable during F1's motion. From the fitting results, we can find that the oscillation periods in three directions are respectively 530 s, 520 s and 521 s, with an average value of 524 s. Obviously, this period is consistent with its vertical oscillation that obtained from the Doppler images. From Figure 7, one can find that the oscillation pattern is the most significant along the slice 7, which is almost perpendicular to the local filament spine. That fact that the direction of the most significant oscillation is perpendicular to the filament spine implies that the filament oscillation is a horizontal oscillation.

B. MEASUREMENT OF THE FILAMENTS' LENGTH

In actual observations, a solar filament should have a real 3D structure with variations in height. To comprehensively analyze the 3D length of a solar filament, stereoscopic observations from at least two different perspectives are required ([Tan et al. 2023](#)). However, currently, only single perspective observations from the Earth are available. Therefore, we assume that the solar filament has no height variations, that is, the solar filament is distributed on a spherical surface with a fixed radius (the solar surface). Assuming that filaments F1 and F2 are uniform cylinders, we select 10 points uniformly along their axes from one endpoint to another respectively (in helioprojective cartesian (HPC) coordinates). Using the functions in the *astropy* and *sunpy* libraries in Python, we convert the HPC coordinates of these ten points into heliographic Stonyhurst (HGS) coordinates. Keeping the longitude and latitude unchanged, the radius is adjusted to the solar radius R_{\odot} . We apply the formula for converting spherical

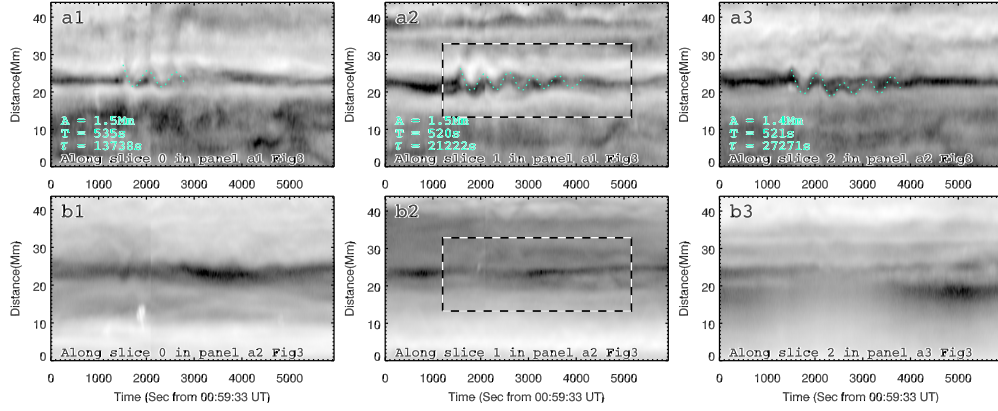


Figure 6. The time-distance stack plots for filaments F1 and F3 along the slices marked 0, 1 and 2 in panels a1 and a3 of Figure 3, using the AIA 171 Å raw images. The green curves in top row are the oscillation curves that manually marked the positions using for fitting, and the fitting results are listed in corresponding panels. The boxes are the FOV of panel b1 and b3 in Figure 3.

coordinates to Cartesian coordinates to transform the new HGS coordinates into 3D Cartesian coordinates (output the value of x , y , z in units of the solar radius R_{\odot} , and finally take R_{\odot} as 696.34 Mm). Lastly, we calculate the corresponding distances using the x , y , z values of every two adjacent points. Summing up the spacings of the 10 sample points yields the estimated length of the filament. This approximation method can yield the most optimal estimation results under the current observational condition. Although it will generate certain errors, these errors are acceptable because the variation in the height of the solar filament is not significant.

C. ACKNOWLEDGMENTS

We would like to thank Prof. Pengfei Chen in Nanjing University, Dr. Song Tan in Leibniz-Institut für Astrophysik Potsdam (AIP) and Dr. Qingmin Zhang in Purple Mountain Observatory of the Chinese Academy of Sciences for valuable discussions and suggestions. This paper utilized data from SDO, SMART, SUTRI and CHASE. This work is supported by the Natural Science Foundation of China (12303062, 12373063, 12103016), the Sichuan Science and Technology Program (2023NSFSC1351, 2025ZNSFSC0315), the Project Supported by the Specialized Research Fund for State Key Laboratories, Key Laboratory of Detection and Application of Space Effect in Southwest Sichuan at Leshan Normal University, Education Department of Sichuan Province (No.ZDXM20241002), and the Fund of Shenzhen Institute of Information Technology (SZIIT2025KJ003, HX-0951). We also acknowledge Sichuan Normal University Astrophysical Laboratory Supercomputer for providing the computational resources.

REFERENCES

- Arregui, I., Oliver, R., & Ballester, J. L. 2018, *Living Reviews in Solar Physics*, 15, 3, doi: [10.1007/s41116-018-0012-6](https://doi.org/10.1007/s41116-018-0012-6)
- Asai, A., Ishii, T. T., Isobe, H., et al. 2012, *ApJL*, 745, L18, doi: [10.1088/2041-8205/745/2/L18](https://doi.org/10.1088/2041-8205/745/2/L18)
- Bai, X., Tian, H., Deng, Y., et al. 2023, *Research in Astronomy and Astrophysics*, 23, 065014, doi: [10.1088/1674-4527/accc74](https://doi.org/10.1088/1674-4527/accc74)
- Balthasar, H., Wiehr, E., Schleicher, H., & Wohl, H. 1993, *A&A*, 277, 635
- Beckers, J. M. 1964, PhD thesis, University of Utrecht, Netherlands
- Berger, T. E., Shine, R. A., Slater, G. L., et al. 2008, *ApJL*, 676, L89, doi: [10.1086/587171](https://doi.org/10.1086/587171)
- Bi, Y., Jiang, Y., Yang, J., et al. 2014, *ApJ*, 790, 100, doi: [10.1088/0004-637X/790/2/100](https://doi.org/10.1088/0004-637X/790/2/100)
- Chen, J., Xie, W., Zhou, Y., et al. 2017, *Ap&SS*, 362, 165, doi: [10.1007/s10509-017-3140-x](https://doi.org/10.1007/s10509-017-3140-x)
- Chen, P. 2023a, *Science China Physics, Mechanics, and Astronomy*, 66, 129631, doi: [10.1007/s11433-023-2228-8](https://doi.org/10.1007/s11433-023-2228-8)
- Chen, P. F. 2006, *ApJL*, 641, L153, doi: [10.1086/503868](https://doi.org/10.1086/503868)
- . 2009, *ApJL*, 698, L112, doi: [10.1088/0004-637X/698/2/L112](https://doi.org/10.1088/0004-637X/698/2/L112)
- . 2023b, *Reviews of Geophysics and Planetary Physics*, 54, 355, doi: [10.19975/j.dqyxx.2022-066](https://doi.org/10.19975/j.dqyxx.2022-066)
- Chen, P. F., Fang, C., & Shibata, K. 2005, *ApJ*, 622, 1202, doi: [10.1086/428084](https://doi.org/10.1086/428084)
- Chen, P. F., Wu, S. T., Shibata, K., & Fang, C. 2002, *ApJL*, 572, L99, doi: [10.1086/341486](https://doi.org/10.1086/341486)
- Chen, P. F., & Wu, Y. 2011, *ApJL*, 732, L20, doi: [10.1088/2041-8205/732/2/L20](https://doi.org/10.1088/2041-8205/732/2/L20)

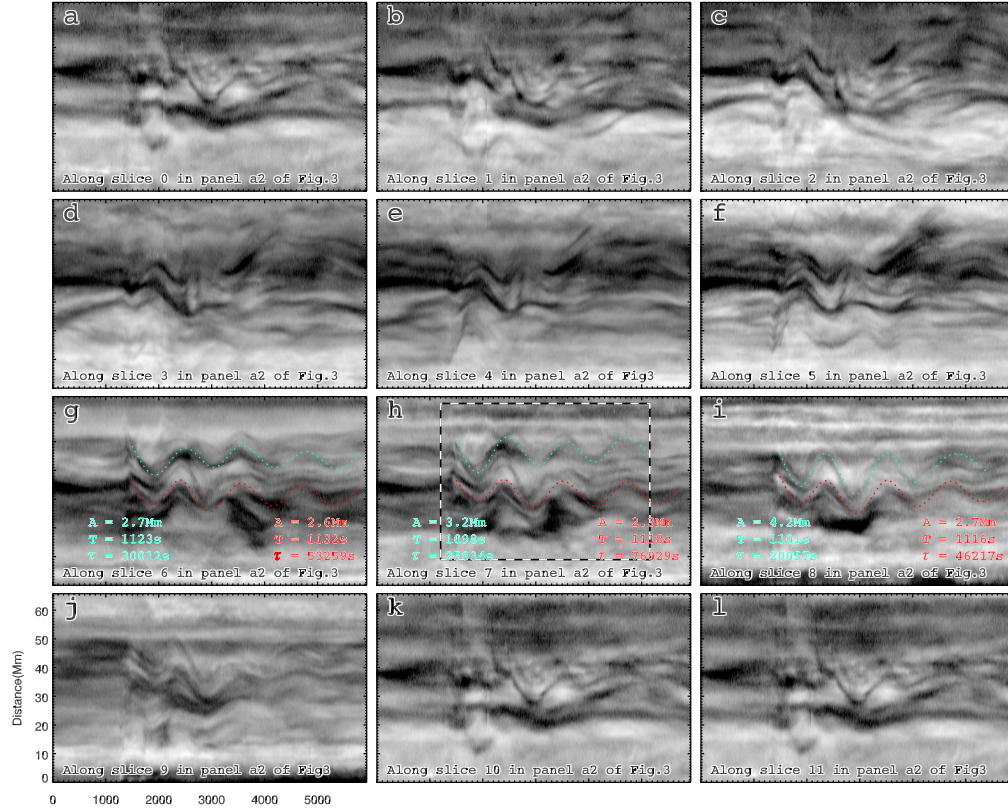


Figure 7. Time-distance stack plots are generated for 12 slices in Figure 3 a2, with each slice spaced at 15° intervals and centered on the filament mass F2, using 171 \AA raw images. Third row is the oscillation of filament F2 in the directions slice 6, 7 and 8 in Figure 3 panel a2, where the green and red curves are the oscillation curve that manually marked the positions using fore fitting and their corresponding fitting results are listed with corresponding colors in each panel. The box in panel S7 is the Fov for Figure 3 b2.

Chen, Y., Hu, J., Cheng, G., et al. 2024, ApJL, 977, L26,
doi: [10.3847/2041-8213/ad94ea](https://doi.org/10.3847/2041-8213/ad94ea)

Chen, Y., Ye, J., Mei, Z., et al. 2022, ApJ, 933, 148,
doi: [10.3847/1538-4357/ac73ef](https://doi.org/10.3847/1538-4357/ac73ef)

Cheng, X., Zhang, J., Olmedo, O., et al. 2012, ApJL, 745, L5,
doi: [10.1088/2041-8205/745/1/L5](https://doi.org/10.1088/2041-8205/745/1/L5)

Dai, J., Zhang, Q., Qiu, Y., et al. 2023, ApJ, 959, 71,
doi: [10.3847/1538-4357/ad0839](https://doi.org/10.3847/1538-4357/ad0839)

Delaboudinière, J. P., Artzner, G. E., Brunaud, J., et al. 1995, SoPh, 162, 291, doi: [10.1007/BF00733432](https://doi.org/10.1007/BF00733432)

Eto, S., Isobe, H., Narukage, N., et al. 2002, PASJ, 54, 481,
doi: [10.1093/pasj/54.3.481](https://doi.org/10.1093/pasj/54.3.481)

Gilbert, H. R., Daou, A. G., Young, D., Tripathi, D., & Alexander, D. 2008, ApJ, 685, 629, doi: [10.1086/590545](https://doi.org/10.1086/590545)

Gosain, S., & Foullon, C. 2012, ApJ, 761, 103,
doi: [10.1088/0004-637X/761/2/103](https://doi.org/10.1088/0004-637X/761/2/103)

Harra, L. K., Sterling, A. C., Gömöry, P., & Veronig, A. 2011, ApJL, 737, L4, doi: [10.1088/2041-8205/737/1/L4](https://doi.org/10.1088/2041-8205/737/1/L4)

Hershaw, J., Foullon, C., Nakariakov, V. M., & Verwichte, E. 2011, A&A, 531, A53, doi: [10.1051/0004-6361/201116750](https://doi.org/10.1051/0004-6361/201116750)

Hou, Z., Tian, H., Wang, J.-S., et al. 2022, ApJ, 928, 98,
doi: [10.3847/1538-4357/ac590d](https://doi.org/10.3847/1538-4357/ac590d)

Hyder, C. L. 1966, ZA, 63, 78

Ishii, T. T., Kawate, T., Nakatani, Y., et al. 2013, PASJ, 65, 39,
doi: [10.1093/pasj/65.2.39](https://doi.org/10.1093/pasj/65.2.39)

Isobe, H., & Tripathi, D. 2006, A&A, 449, L17,
doi: [10.1051/0004-6361:20064942](https://doi.org/10.1051/0004-6361:20064942)

Kleczeck, J., & Kuperus, M. 1969, SoPh, 6, 72,
doi: [10.1007/BF00146797](https://doi.org/10.1007/BF00146797)

Labrosse, N., Heinzel, P., Vial, J. C., et al. 2010, SSRv, 151, 243,
doi: [10.1007/s11214-010-9630-6](https://doi.org/10.1007/s11214-010-9630-6)

Lemen, J. R., Tittle, A. M., Akin, D. J., et al. 2012, SoPh, 275, 17,
doi: [10.1007/s11207-011-9776-8](https://doi.org/10.1007/s11207-011-9776-8)

Li, C., Fang, C., Li, Z., et al. 2019, Research in Astronomy and Astrophysics, 19, 165, doi: [10.1088/1674-4527/19/11/165](https://doi.org/10.1088/1674-4527/19/11/165)

—. 2022, Science China Physics, Mechanics, and Astronomy, 65, 289602, doi: [10.1007/s11433-022-1893-3](https://doi.org/10.1007/s11433-022-1893-3)

Li, D., Bai, X., Tian, H., et al. 2023, A&A, 675, A169,
doi: [10.1051/0004-6361/202245812](https://doi.org/10.1051/0004-6361/202245812)

Li, T., & Zhang, J. 2012, ApJL, 760, L10,
doi: [10.1088/2041-8205/760/1/L10](https://doi.org/10.1088/2041-8205/760/1/L10)

- Li, T., Zhang, J., Yang, S., & Liu, W. 2012, *ApJ*, 746, 13, doi: [10.1088/0004-637X/746/1/13](https://doi.org/10.1088/0004-637X/746/1/13)
- Liakh, V., & Keppens, R. 2023, *ApJL*, 953, L13, doi: [10.3847/2041-8213/acea78](https://doi.org/10.3847/2041-8213/acea78)
- . 2025, *A&A*, 696, A158, doi: [10.1051/0004-6361/202453300](https://doi.org/10.1051/0004-6361/202453300)
- Liakh, V., Luna, M., & Khomenko, E. 2020, *A&A*, 637, A75, doi: [10.1051/0004-6361/201937083](https://doi.org/10.1051/0004-6361/201937083)
- . 2021, *A&A*, 654, A145, doi: [10.1051/0004-6361/202141524](https://doi.org/10.1051/0004-6361/202141524)
- . 2023, *A&A*, 673, A154, doi: [10.1051/0004-6361/202245765](https://doi.org/10.1051/0004-6361/202245765)
- Liu, R., Liu, C., Xu, Y., et al. 2013, *ApJ*, 773, 166, doi: [10.1088/0004-637X/773/2/166](https://doi.org/10.1088/0004-637X/773/2/166)
- Liu, W., Ofman, L., Nitta, N. V., et al. 2012, *ApJ*, 753, 52, doi: [10.1088/0004-637X/753/1/52](https://doi.org/10.1088/0004-637X/753/1/52)
- Luna, M., Joshi, R., Schmieder, B., et al. 2024, *A&A*, 691, A354, doi: [10.1051/0004-6361/202450869](https://doi.org/10.1051/0004-6361/202450869)
- Luna, M., & Karpen, J. 2012, *ApJL*, 750, L1, doi: [10.1088/2041-8205/750/1/L1](https://doi.org/10.1088/2041-8205/750/1/L1)
- Luna, M., Karpen, J., Ballester, J. L., et al. 2018, *ApJS*, 236, 35, doi: [10.3847/1538-4365/aabde7](https://doi.org/10.3847/1538-4365/aabde7)
- Luna, M., Knizhnik, K., Muglach, K., et al. 2014, *ApJ*, 785, 79, doi: [10.1088/0004-637X/785/1/79](https://doi.org/10.1088/0004-637X/785/1/79)
- Luna, M., Su, Y., Schmieder, B., Chandra, R., & Kucera, T. A. 2017, *ApJ*, 850, 143, doi: [10.3847/1538-4357/aa9713](https://doi.org/10.3847/1538-4357/aa9713)
- Ma, S., Raymond, J. C., Golub, L., et al. 2011, *ApJ*, 738, 160, doi: [10.1088/0004-637X/738/2/160](https://doi.org/10.1088/0004-637X/738/2/160)
- Mazumder, R., Pant, V., Luna, M., & Banerjee, D. 2020, *A&A*, 633, A12, doi: [10.1051/0004-6361/201936453](https://doi.org/10.1051/0004-6361/201936453)
- Miao, Y., Liu, Y., Elmhamdi, A., et al. 2020, *ApJ*, 889, 139, doi: [10.3847/1538-4357/ab655f](https://doi.org/10.3847/1538-4357/ab655f)
- Miao, Y. H., Liu, Y., Shen, Y. D., et al. 2019, *ApJL*, 871, L2, doi: [10.3847/2041-8213/aafaf9](https://doi.org/10.3847/2041-8213/aafaf9)
- Moreton, G. E. 1960, *AJ*, 65, 494, doi: [10.1086/108346](https://doi.org/10.1086/108346)
- Newton, H. W. 1935, *MNRAS*, 95, 650, doi: [10.1093/mnras/95.8.650](https://doi.org/10.1093/mnras/95.8.650)
- Okamoto, T. J., Nakai, H., Keiyama, A., et al. 2004, *ApJ*, 608, 1124, doi: [10.1086/420838](https://doi.org/10.1086/420838)
- Ouyang, W., Liang, H., Yu, K., Zhou, X., & Miao, Y. 2025, *Physics of Fluids*, 37, 037177, doi: [10.1063/5.0257443](https://doi.org/10.1063/5.0257443)
- Pesnell, W. D., Thompson, B. J., & Chamberlin, P. C. 2012, *SoPh*, 275, 3, doi: [10.1007/s11207-011-9841-3](https://doi.org/10.1007/s11207-011-9841-3)
- Ramsey, H. E., & Smith, S. F. 1966, *AJ*, 71, 197, doi: [10.1086/109903](https://doi.org/10.1086/109903)
- Shen, Y., Ichimoto, K., Ishii, T. T., et al. 2014a, *ApJ*, 786, 151, doi: [10.1088/0004-637X/786/2/151](https://doi.org/10.1088/0004-637X/786/2/151)
- Shen, Y., Liu, Y. D., Chen, P. F., & Ichimoto, K. 2014b, *ApJ*, 795, 130, doi: [10.1088/0004-637X/795/2/130](https://doi.org/10.1088/0004-637X/795/2/130)
- Srivastava, A. K., Dwivedi, B. N., & Kumar, M. 2013, *Ap&SS*, 345, 25, doi: [10.1007/s10509-013-1361-1](https://doi.org/10.1007/s10509-013-1361-1)
- Srivastava, A. K., & Goossens, M. 2013, *ApJ*, 777, 17, doi: [10.1088/0004-637X/777/1/17](https://doi.org/10.1088/0004-637X/777/1/17)
- Tan, S., Shen, Y., Zhou, X., et al. 2022, *MNRAS*, 516, L12, doi: [10.1093/mnras/516/1/L12](https://doi.org/10.1093/mnras/516/1/L12)
- . 2023, *MNRAS*, 520, 3080, doi: [10.1093/mnras/stad295](https://doi.org/10.1093/mnras/stad295)
- Terradas, J., Molowny-Horas, R., Wiehr, E., et al. 2002, *A&A*, 393, 637, doi: [10.1051/0004-6361:20020967](https://doi.org/10.1051/0004-6361:20020967)
- Thompson, B. J., Plunkett, S. P., Gurman, J. B., et al. 1998, *Geophys. Res. Lett.*, 25, 2465, doi: [10.1029/98GL50429](https://doi.org/10.1029/98GL50429)
- Tian, H. 2017, *Research in Astronomy and Astrophysics*, 17, 110, doi: [10.1088/1674-4527/17/11/110](https://doi.org/10.1088/1674-4527/17/11/110)
- Tripathi, D., Isobe, H., & Jain, R. 2009, *SSRv*, 149, 283, doi: [10.1007/s11214-009-9583-9](https://doi.org/10.1007/s11214-009-9583-9)
- Tsubaki, T., & Takeuchi, A. 1986, *SoPh*, 104, 313, doi: [10.1007/BF00159084](https://doi.org/10.1007/BF00159084)
- Uchida, Y. 1968, *SoPh*, 4, 30, doi: [10.1007/BF00146996](https://doi.org/10.1007/BF00146996)
- UeNo, S., Nagata, S.-i., Kitai, R., Kurokawa, H., & Ichimoto, K. 2004, in *Society of Photo-Optical Instrumentation Engineers (SPIE) Conference Series*, Vol. 5492, Ground-based Instrumentation for Astronomy, ed. A. F. M. Moorwood & M. Iye, 958–969, doi: [10.1117/12.550304](https://doi.org/10.1117/12.550304)
- Veronig, A. M., Gömöry, P., Kienreich, I. W., et al. 2011, *ApJL*, 743, L10, doi: [10.1088/2041-8205/743/1/L10](https://doi.org/10.1088/2041-8205/743/1/L10)
- Wang, C., Chen, F., & Ding, M. 2021, *ApJL*, 911, L8, doi: [10.3847/2041-8213/abefe6](https://doi.org/10.3847/2041-8213/abefe6)
- Wang, J., Yan, X., Kong, D., et al. 2020, *ApJ*, 894, 30, doi: [10.3847/1538-4357/ab8565](https://doi.org/10.3847/1538-4357/ab8565)
- Wang, X., Zheng, R., Liu, Y., et al. 2025, *ApJ*, 980, 254, doi: [10.3847/1538-4357/adb035](https://doi.org/10.3847/1538-4357/adb035)
- Warmuth, A., Vršnak, B., Aurass, H., & Hanslmeier, A. 2001, *ApJL*, 560, L105, doi: [10.1086/324055](https://doi.org/10.1086/324055)
- Yan, X., Xue, Z., Wang, J., et al. 2025, *ApJ*, 981, 139, doi: [10.3847/1538-4357/adb39e](https://doi.org/10.3847/1538-4357/adb39e)
- Zhang, Q., Li, C., Li, D., et al. 2022, *ApJL*, 937, L21, doi: [10.3847/2041-8213/ac8e01](https://doi.org/10.3847/2041-8213/ac8e01)
- Zhang, Q. M. 2020, *A&A*, 642, A159, doi: [10.1051/0004-6361/202038557](https://doi.org/10.1051/0004-6361/202038557)
- Zhang, Q. M., Chen, P. F., Xia, C., & Keppens, R. 2012, *A&A*, 542, A52, doi: [10.1051/0004-6361/201218786](https://doi.org/10.1051/0004-6361/201218786)
- Zhang, Q. M., Chen, P. F., Xia, C., Keppens, R., & Ji, H. S. 2013, *A&A*, 554, A124, doi: [10.1051/0004-6361/201220705](https://doi.org/10.1051/0004-6361/201220705)
- Zhang, Q. M., Dai, J., Xu, Z., et al. 2020a, *A&A*, 638, A32, doi: [10.1051/0004-6361/202038233](https://doi.org/10.1051/0004-6361/202038233)
- Zhang, Q. M., Guo, J. H., Tam, K. V., & Xu, A. A. 2020b, *A&A*, 635, A132, doi: [10.1051/0004-6361/201937291](https://doi.org/10.1051/0004-6361/201937291)
- Zhang, Q. M., & Ji, H. S. 2018, *ApJ*, 860, 113, doi: [10.3847/1538-4357/aac37e](https://doi.org/10.3847/1538-4357/aac37e)
- Zhang, Q. M., Li, D., & Ning, Z. J. 2017a, *ApJ*, 851, 47, doi: [10.3847/1538-4357/aa9898](https://doi.org/10.3847/1538-4357/aa9898)
- Zhang, Q. M., Li, T., Zheng, R. S., Su, Y. N., & Ji, H. S. 2017b, *ApJ*, 842, 27, doi: [10.3847/1538-4357/aa73d2](https://doi.org/10.3847/1538-4357/aa73d2)

- Zhang, Q. M., Lin, M. S., Yan, X. L., et al. 2024, MNRAS, 533, 3255, doi: [10.1093/mnras/stae1936](https://doi.org/10.1093/mnras/stae1936)
- Zheng, R., Liu, Y., Liu, W., et al. 2023, ApJL, 949, L8, doi: [10.3847/2041-8213/acd0ac](https://doi.org/10.3847/2041-8213/acd0ac)
- Zhou, X., Shen, Y., Liang, H., et al. 2022a, ApJ, 941, 59, doi: [10.3847/1538-4357/aca1b6](https://doi.org/10.3847/1538-4357/aca1b6)
- Zhou, X., Shen, Y., Su, J., et al. 2021, SoPh, 296, 169, doi: [10.1007/s11207-021-01913-2](https://doi.org/10.1007/s11207-021-01913-2)
- Zhou, X., Shen, Y., Tang, Z., et al. 2022b, A&A, 659, A164, doi: [10.1051/0004-6361/202142536](https://doi.org/10.1051/0004-6361/202142536)
- Zhou, X., Shen, Y., Zhou, C., Tang, Z., & Ibrahim, A. A. 2024a, Science China Physics, Mechanics, and Astronomy, 67, 259611, doi: [10.1007/s11433-023-2309-5](https://doi.org/10.1007/s11433-023-2309-5)
- Zhou, X., Tang, Z., Qu, Z., et al. 2024b, ApJL, 974, L3, doi: [10.3847/2041-8213/ad7a68](https://doi.org/10.3847/2041-8213/ad7a68)
- Zhou, X., Shen, Y., Liu, Y. D., et al. 2022c, ApJL, 930, L5, doi: [10.3847/2041-8213/ac651e](https://doi.org/10.3847/2041-8213/ac651e)
- Zhou, X., Shen, Y., Yan, Y., et al. 2024c, ApJ, 968, 85, doi: [10.3847/1538-4357/ad4456](https://doi.org/10.3847/1538-4357/ad4456)
- Zhou, X., Shen, Y., Yuan, D., et al. 2024d, Nature Communications, 15, 3281, doi: [10.1038/s41467-024-46846-z](https://doi.org/10.1038/s41467-024-46846-z)
- Zhang, X., Chen, H., Zhou, G., et al. 2025, ApJL, 987, L3, doi: [10.3847/2041-8213/ade38c](https://doi.org/10.3847/2041-8213/ade38c)